Physical Characteristics of Unstructured Coronal Clouds

M. Asgari-Targhi[1] , L. Golub[1] , M. Hahn[2] , N. Karna[1] , and D. W. Savin[2]
[1] Harvard-Smithsonian Center for Astrophysics, 60 Garden Street, Cambridge, MA 02138, USA
[2] Columbia Astrophysics Laboratory, Columbia University, 550 West 120th Street, New York, NY 10027, USA

Abstract

Active regions in the inner solar corona, when observed in X-ray emission, consist of bright, hot loops surrounded by unstructured clouds. The emission from the clouds extends to a height of ≈ 4–5×10^4 km at temperatures of ≈ 2–3 MK. These "hot clouds" are variable, but persist for many days and do not appear to connect directly to the active region streamers or other large-scale structures observed higher in the corona. We present an observational analysis of these diffuse structures to establish basic plasma parameters such as magnetic field strength, particle density, and temperature. The values of β, the ratio of the plasma pressure to the magnetic field pressure, were found to be generally less than unity, though often approaching unity in the upper portions of the active region, where the hot clouds are located. The magnetic field may therefore only partially confine these regions and inhibit flare-like instabilities that could otherwise be driven by gradients of plasma pressure and current density.

Unified Astronomy Thesaurus concepts: The Sun (1693)

Supporting material: animation

1. Introduction

Since the late 1960s, on-disk X-ray images of the solar corona have confirmed that the coronal emission is dominated by filamentary loop and arch structures corresponding to closed magnetic fields connecting opposite-polarity bipolar regions on the solar surface (Reidy et al. 1968; Craig et al. 1978; Rosner et al. 1978; Vaiana & Rosner 1978). The launch of the Hinode X-ray Telescope (XRT) has provided an unprecedented opportunity to explore this paradigm by conducting a broad range of high temporal and spatial resolution coronal studies over an extended time, with targets ranging from the quiet Sun to solar flares (Golub et al. 2007). The Hinode observations confirmed the notion that active regions comprise an assemblage of closed loops. However, the problem of connecting the active regions to the higher-lying structures seen at heights > 4–5×10^4 km in the corona, e.g., in white-light eclipse or coronagraph images, has produced puzzling results. The difficulty has been noted when attempting to connect the observed surface fields to the structures seen in the low corona (Gudiksen & Nordlund 2005; Cranmer & Winebarger 2019), and the present study indicates that a similar difficulty is also present in the corona above the compact core loops in active regions.

Here, we explore the properties of the emission above active region core loops, at heights upward of $\sim 0.05\, R_\odot$ ($\sim 3.5 \times 10^4$ km) above the solar surface. What is frequently seen is presented in Figure 1, which shows images obtained with the Hinode XRT of the emission in the upper portions of two different active regions. The emission above the core loops of the two active regions is less bright than the core loops and is best seen when the regions approach the solar limb. We find that this emission appears diffuse and cloud like and does not exhibit the expected increasingly large and faint series of closed loops. Because these regions are seen in a grazing-incidence X-ray telescope, they are at a temperature of several million Kelvin (as detailed in Section 3 below), and we will refer to these diffuse regions as "hot clouds." The goal of the present study is to establish the basic observable properties of

these hot clouds (Sections 2 and 3). We discuss the possible implications for coronal physics in the concluding discussion (Section 4).

2. Observations

We examine active regions NOAA 10938 and NOAA 10939 observed in 2007 January using XRT (Golub et al. 2007) on board the Hinode spacecraft (Kosugi et al. 2007). Synoptic full-disk Al-poly images taken during the disk passage of AR 10938 from 2007 January 11 to 22 were used in order to determine the active regions to be studied, as well as to establish the presence and locations of the hot clouds. A sequence of cutout images showing midlatitude frames during the disk passage is presented in Figure 2. Fortuitously, AR 10939 emerged on the disk on January 16 and grew rapidly, with a hot cloud observed above the core loops by the time it approached the limb on January 22, thereby establishing that hot clouds form early in the evolution of an active region.

A targeted set of XRT Al-poly images centered on these two regions was obtained on 2007 January 24, from 01:57:00 UT through 09:12:00 UT with a cadence averaging ≈ 4 minutes, and an animation of the January 24 high-cadence observation is presented in Figure 3. The animation shows the unstructured nature of the clouds as well as swirling motions on timescales of minutes within a stable configuration that remains largely unchanged for the ≈ 8 hr duration of the observing sequence. The clouds reach a height of ≈ 4–5×10^4 km at temperatures of ≈ 2–3 MK.

To assist in interpreting these X-ray observations, we have used line-of-sight magnetograms taken on 2007 January 18 at 19:15:35 UT and 2007 January 22 at 00:03:30 UT by the Michelson Doppler Imager (MDI) on board the Solar and Heliospheric Observatory (SOHO; Scherrer et al. 1995) to model the magnetic structures of these two regions.

We first compute the potential field for the observed regions employing the relevant IDL and Fortran software codes known as the Coronal Modeling System (CMS; van Ballegooijen 2004; Asgari-Targhi & van Ballegooijen 2012;
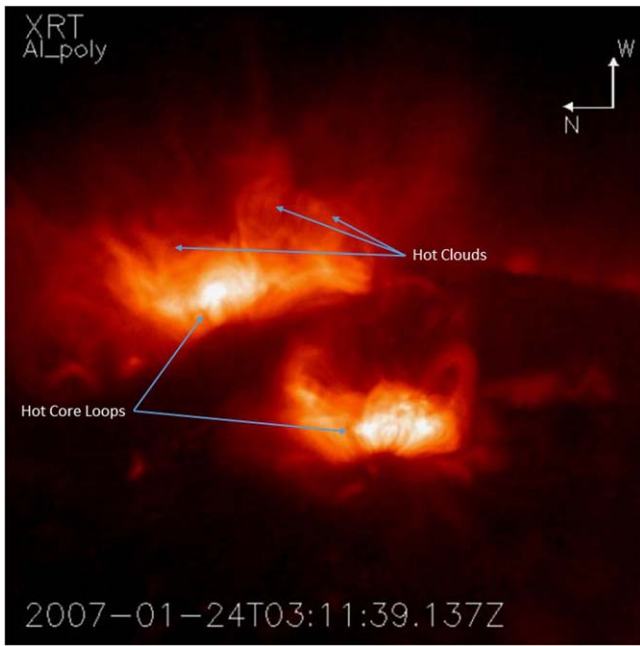
Figure 1. An XRT Al-Poly image of active regions NOAA 10938 at the limb and 10939 approaching the limb, observed on 2007 January 24. The cloud-like hot material above the bright core loops becomes more easily visible in X-ray images when the active region is at the limb. Arrows point to the hot inner core loops of the two active regions, and to some examples of the cloud-like emissions above the core loops.

Asgari-Targhi et al. 2013). A magnetic potential field is equivalent to a current-free field; therefore, the current density $J = 0$. We create the potential field model of this region using the MDI magnetogram and the MDI synoptic map for Carrington rotation 2052.

Some of the observed field lines showed deviations from the potential field and cannot be fitted accurately with a potential field model. We used CMS to account for this. With the IDL portion of CMS, we are able (1) to construct potential field models, (2) to set up the initial conditions for nonpotential field models such as including current or inserting flux rope(s) into a potential field, (3) to visualize the modeling results by plotting field lines, and (4) to make detailed visual comparisons of the models with relevant images such as XRT images, which we discuss below. The Fortran portion of CMS enables us to perform magnetofrictional relaxation of nonpotential models to produce nonlinear force-free fields (NLFFF).

Using CMS, we modeled the magnetic field by applying an NLFFF model to the observed active regions. In the NLFFF model, the nonmagnetic forces are negligible, and because the electric current flows parallel to the magnetic field, the Lorentz force also vanishes, i.e., $J \times B = 0$, where B is the magnetic field. Our magnetic field modeling of this region was constrained by the position of the active regions and the availability of the MDI magnetograms. We will use the magnetic field measurements presented here to compute the plasma-β parameter in Section 2.1. The plasma β will help us to understand the role of the magnetic field in confining the clouds formed above the coronal loops.

Figure 2 shows a series of XRT images of the active region NOAA 10938 observed from 2007 January 11 to 2007 January 22. The second active region, NOAA 10939, is first viewed on 2007 January 20. Based on the position of the active regions on 2007 January 22 (the last panel of Figure 2), they would be

close to the limb on January 24 and farther from the disk center. The NLFFF model does not provide a good approximation for active regions near the limb (De Rosa et al. 2009). Consequently, we cannot use magnetogram data from the same day as our 2007 January 24 XRT data. Instead, we used MDI observations taken on 2007 January 18 and 2007 January 22, where the active regions are closer to the disk center, and the MDI observations are available. By using two days separated in time, we can also assess the evolution of the active region.

Figure 4(a) shows the full-disk MDI magnetogram observed on 2007 January 18 at 19:15:35 UT. Figure 4(b) shows the large sunspot characterizing the active region NOAA 10938. The fitted field lines are traced through the 3D NLFFF model, described below, and connect positive and negative polarities, shown with red and green contours, respectively. Figure 4(c) shows the active region NOAA 10938 observed by the Extreme-ultraviolet Imaging Telescope (EIT) on board SOHO in 304 Å on 2007 January 18 at 11:19:37 UT with a filament present in the area surrounding it. The existence of a filament in this region is evidence of nonpotentiality and suggests that we need to use the NLFFF model to fit magnetic field lines to the observed loops.

One method for constructing the NLFFF is to extrapolate the observed photospheric vector field into the corona (see De Rosa et al. 2009 and references therein). In our approach, we use the line-of-sight magnetogram and the observed shapes of the sheared loops or Hα filaments to constrain the NLFFF model. This approach has been successfully applied to studies of filaments (van Ballegooijen 2004), active regions (Bobra et al. 2008; Su et al. 2009a, 2009b, 2011), coronal X-ray sigmoids (Savcheva & van Ballegooijen 2009), and loops (Asgari-Targhi & van Ballegooijen 2012; Asgari-Targhi et al. 2013, 2014). It uses the "flux rope insertion method" to model the active region, where a magnetic flux rope is inserted into a potential field model of the region of interest (ROI), and magnetofrictional relaxation is then applied to construct the NLFFF extrapolation. This method is quite flexible and provides information about the stability of the resulting field lines.

A few of the field lines in our study showed small deviations from the potential field model, consistent with the existence of a filament in this active region. To correct these deviations, we inserted an untwisted flux bundle with an axial flux of 10^{20} Mx. We then applied magnetofrictional relaxation to the configuration until an NLFFF model was obtained after 60,000 iterations. The resulting NLFFF model fits the observed coronal loops. We traced a series of magnetic field lines through the 3D NLFFF model, of which 12 field lines are presented in Figures 4(b) and (d). The XRT image is taken using the A1-poly filter and shows the field lines fitted to the observed coronal loops emanating from the sunspot and the enclosing areas.

We studied the magnetic field $B(s)$ variation as a function of position s along the loop for all the fitted field lines. Figure 5 shows the plots for two of the field lines. The magnetic field at the top of the field line numbered 42 is 6.78 G. The magnetic field at the top of the shortest fitted loop, identified as 48, is 22 G. The magnetic field variation at the top of the fitted field lines in this region is 6–22 G.

We now turn to the observations made a few days later on 2007 January 22 as shown in Figure 6. Figure 6(a) shows the full-disk MDI magnetogram observed at 00:03:30 UT.
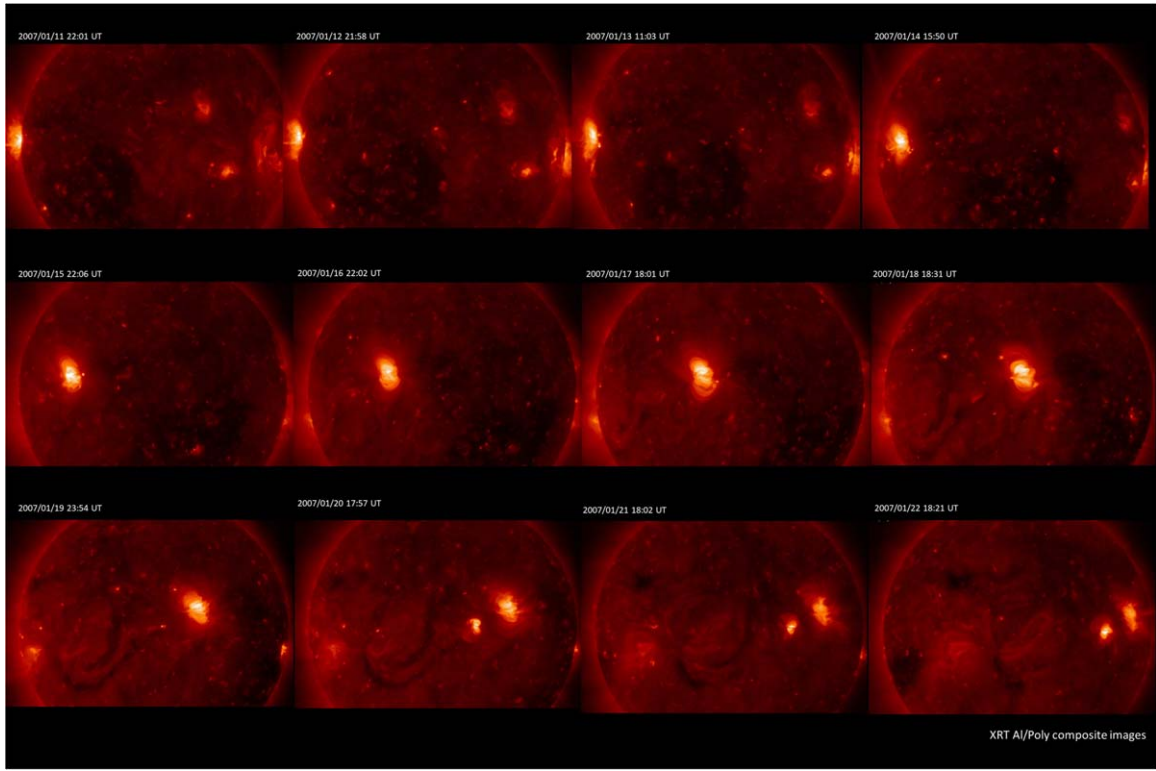
Figure 2. A sequence of full-disk XRT Al-poly synoptic images of the active region NOAA 10938 observed from 2007 January 11 to 2007 January 22. Note that the active region NOAA 10939 appears on 2007 January 20. The images are composites made from long–short exposure pairs, with exposure times determined by the (varying) pixel intensity distributions in the images.

Figure 6(b) shows two sunspots characterizing the active regions NOAA 10938 (top right) and NOAA 10939 (lower left). The 3D NLFFF is used to trace field lines connecting positive and negative polarities, shown with red and green contours, respectively. Figure 6(c) shows the active regions observed by EIT/SOHO in 304 Å at 01:19:40 UT. The image confirms that a filament is passing through the upper active region. We constructed the NLFFF model for both active regions observed on this date. Figure 6(d) shows 23 of the field lines fitted to the observed coronal loops in both active regions. We measured the magnetic field strength as a function of position for all these field lines. Figure 7 shows the magnetic field as a function of position for two of the selected field lines. At the top of the shortest modeled loop, numbered 45 in the active region NOAA 10939, the magnetic field is 56 G. The magnetic field strength at the top of the large loop, identified as 37 in the active region NOAA 10938, is 10 G. The changes to the active region structure between 2007 January 18 and 2007 January 22 are very small. So, the uncertainties in estimating the magnetic field strengths in the active region on 2007 January 24 based on the data from January 22 are expected to be small.

2.1. Measurements of the β Parameter

The solar atmosphere has a complex structure due to magnetic and pressure forces that alternate roles for dominance (Gary 2001). The dominating force is defined by the plasma β parameter, which is the ratio of plasma pressure, p, to magnetic pressure,

$$\beta = \frac{p}{B^2/8\pi}. \tag{1}$$

When the plasma pressure dominates over the magnetic pressure, $\beta > 1$. Generally, this happens in the photosphere and the upper corona (see Figure 3 of Gary 2001). However, in the middle corona, the magnetic pressure dominates over the plasma pressure and other nonmagnetic forces such as gravity, and therefore $\beta < 1$.

The plasma pressure $p(s)$, mass density $\rho(s)$, and electron density $n_e(s)$ are given by

$$p = c_1 n_p k_B T, \quad \rho = c_2 m_p n_p, \quad n_e = c_3 n_p, \tag{2}$$

respectively, where $n_p(s)$ is the proton density, k_B is the Boltzmann constant, and T is the proton temperature. Assuming the plasma is fully ionized, the three constants are given by $c_1 = 2 + 3A_{He}$, $c_2 = 1 + 4A_{He}$, and $c_3 = 1 + 2A_{He}$, where A_{He} is the relative helium abundance (Asgari-Targhi & van Ballegooijen 2012). The plasma pressure is computed based on the method introduced in Schrijver & van Ballegooijen (2005) and Appendix A of Asgari-Targhi & van Ballegooijen (2012). We used the magnetic field measurements presented in the previous section to compute the magnetic pressure.

Figure 8(a) shows the β parameter for field line 42 as a function of position along the field line shown in Figure 5(a). The value of β at the top of this loop is about 2. However, as Figure 8(b) shows that the value of β as a function of position for the shorter field line 48, shown in Figure 5(c), is much smaller than 1. The β has a value of 0.11 near the top of field line 48. Figure 9 presents the plasma β parameter as a function of position along the field line for two of the field lines shown in Figures 7(a) and (c). The shorter field line, numbered 45 in Figure 7(a), has a β value approaching 0.01 at its peak, whereas
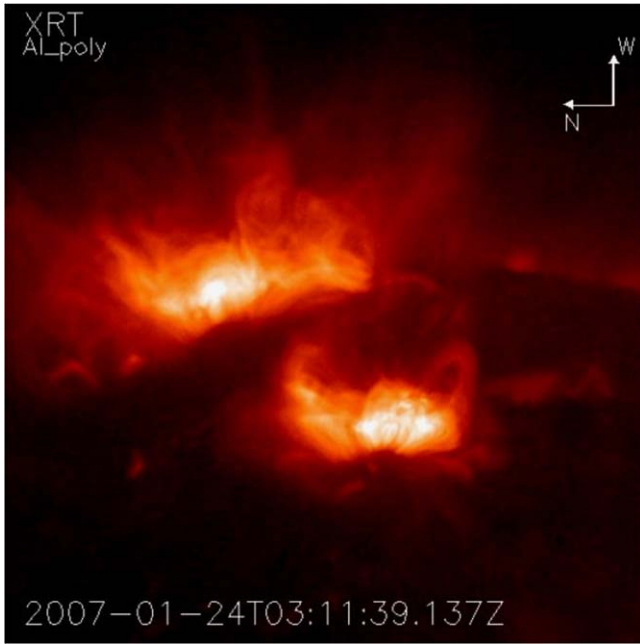
Figure 3. This animation shows a sequence of XRT Al-poly images from an extended (~8 hr) observation of active regions NOAA 10938 and NOAA 10939 observed on 2007 January 24 (01:57 to 10:00 UT). The bright, hot inner core loops are seen low in the corona, and above them are the fainter unstructured cloud-like X-ray emitting regions. In the animation, the latter are seen to slowly swirl and change, with coherent fog-like movement evident on timescales of minutes, the hot plasma apparently not forced to flow along thin closed magnetic field lines present in the lower portions of the active regions. These cloud-like properties are most clearly visible in the older AR 10938 that is closer to the solar limb. The clouds appear to be just beginning to take shape in the younger active region in the foreground of this animation.

(An animation of this figure is available.)

for the longer field line, numbered 37 in Figure 7(c), β reaches close to 1. This confirms that within the same active region, the plasma β parameter varies significantly depending on the position and the length of the field line.

The plasma β measured in the magnetic field lines presented here varies with the position and height of the loops and is mostly less than unity. However, in some coronal loops, such as field line 42 shown here, β exceeds 1. Because the clouds are formed above the coronal loops in the active regions, their plasma β parameter is similar to those measured at the top of the coronal loops. For the cases where the plasma β is less than unity in the upper parts of the active regions, where the hot clouds are located, the magnetic field may confine these clouds.

3. Extreme Ultraviolet Imaging Spectrometer Observations

We also analyzed an observation of these active regions made with the Extreme Ultraviolet Imaging Spectrometer (EIS; Culhane et al. 2007) on Hinode. The observation was made on 2007 January 26 04:03:20 UT using the $1''$ slit of EIS. The field of view consisted of 128 horizontal raster positions spaced $\approx 1''$. For this observation, the slit was $128''$ long in the vertical direction, resulting in a 128×128 pixel image. The exposure time was about 25 s per position so that the total observation lasted about 1 hr. An image of the field of view in Fe XII (Figure 10) shows the active region at the limb of the Sun. For much of our analysis, we are interested in the region above the

active region loops. This ROI is illustrated by the boxed region in Figure 10 and lies $\sim 0.05\, R_\odot$ above the limb.

In order to improve the statistical uncertainties, we performed the analysis using both the full spatial resolution data as well as a binned data set. For this binning, we summed the raw data in 2×2 pixel squares, thereby increasing the effective exposure time by a factor of four. The result was 64×64 bins over the same field of view with $2'' \times 2''$ square bins. Here, we focus on the results of the binned data as it has reduced statistical uncertainties. The reduced spatial resolution did not appear to have any significant effect on the analysis.

The quantities of interest for comparison with theoretical models of active region clouds include the electron temperature T_e, the ion temperature T_i, the gradients of T_e and T_i, the electron density n_e, and the gradient of n_e. Our measurements for these quantities based on the EIS data are described below.

3.1. Electron Temperature

The electron temperature was measured using a differential emission measure (DEM) analysis. The DEM, $\phi(T_e)$, describes the amount of material along the line of sight as a function of temperature. It is related to n_e by

$$n_e^2 = \phi(T_e)\frac{dT_e}{dh},\tag{3}$$

where dh is a length element along the line of sight. The DEM is related to the measured intensities by

$$I_{ji} = \frac{1}{4\pi}\int G_{ji}(T_e)\phi(T_e)dT_e,\tag{4}$$

where I_{ji} represents the intensity of an emission line due to the transition from level j to level i and $G_{ji}(T_e)$ is the contribution function for that transition and contains the relevant atomic data. Given intensities from many different emission lines, Equation (4) can be inverted to determine $\phi(T_e)$. For our analysis, we have used the regularized inversion technique of Hannah & Kontar (2012).

The DEM inversion was performed within each pixel or bin of the field of view using lines from ions formed at a broad range of temperatures from about $\log[T\,(\mathrm{K})] = 5.8$ to 6.7. The line list included Fe VIII–XVII, Si VII, and Si X. The DEM inversion was performed assuming photospheric elemental abundances. It is possible that the coronal elemental abundances differ from the photospheric values due to the first ionization potential (FIP) effect. However, because both Fe and Si are low FIP ions, they are expected to respond to the FIP effect in the same way. So, this uncertainty introduces only a change in the magnitude of the DEM and does not affect the temperature analysis. Ions from S, Ar, and Ca are also available in the spectrum, but may respond differently to the FIP effect and so are omitted from the DEM analysis.

Figure 11 shows an example of the DEM near the center of the off-limb portion of the field of view. The DEM has two peaks within the temperature range constrained by the observed line intensities. One peak is at $\log[T\,(\mathrm{K})] \approx 6.1$ and another at $\log[T\,(\mathrm{K})] \approx 6.3$. This multimodal thermal structure is similar to what has been found previously for active regions (e.g., Landi & Feldman 2008). The lower temperature peak corresponds roughly to the characteristic temperature of the quiet Sun, suggesting that it is due to the quiet-Sun corona in the foreground or background. The higher temperature peak likely represents the temperature of the active region.
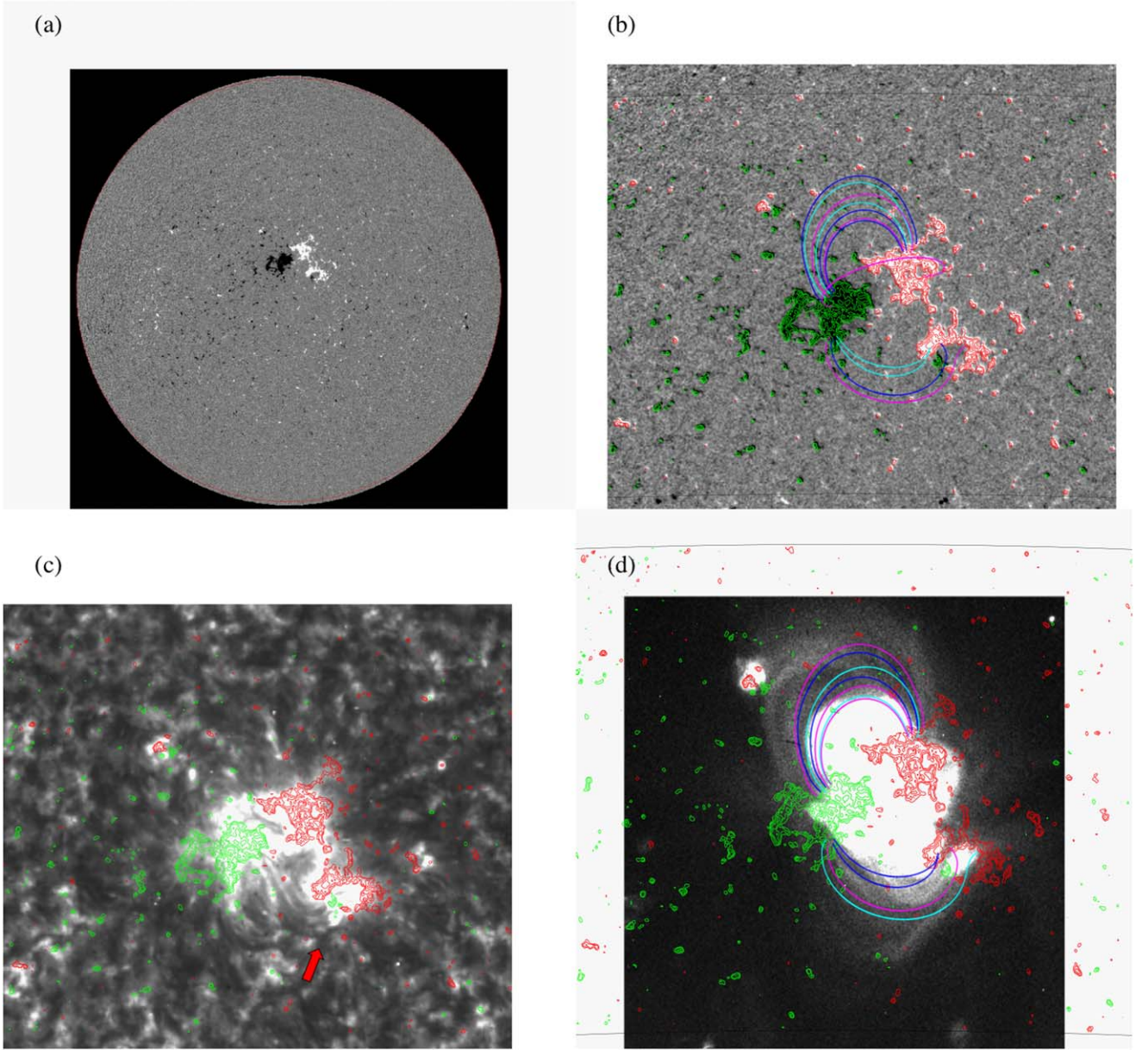
Figure 4. (a) MDI full-disk magnetogram observed on 2007 January 18 at 19:15:35 UT showing regions of positive polarity in white and negative polarity in black. These regions are also shown in red and green, respectively, in panels (b), (c), and (d). (b) NLFFF model of active region NOAA 10938. The curves are randomly selected field lines connecting positive and negative polarities and traced through the 3D model. The colors of the field lines are arbitrary. Multiple field line colors are used to enhance visibility. Selected field lines in panels (b) and (d) are the same set of field lines. (c) The active region NOAA 10938 observed by EIT/SOHO on 2007 January 18 at 11:19:37 UT in 304 Å with the filament (red arrow) passing through it. (d) The randomly selected magnetic field lines traced through the NLFFF model. The background image is an XRT image on 2007 January 18 at 19:19:42 UT taken with the Al-poly filter.

In order to build a map of the temperature within the field of view, we determined the temperature of the hotter peak from the DEM in each observed pixel. Figure 12 maps the temperature of this peak throughout the field of view. Here and throughout when discussing the electron temperature of the observations, we are referring to this hotter peak in the DEM.

3.2. Ion Temperature

The observed width of an optically thin emission line depends on instrumental broadening $\Delta\lambda_{\mathrm{inst}}$, the ion temperature T_{i}, and the nonthermal velocity v_{nt} (Phillips et al. 2008):

$$\Delta\lambda_{\mathrm{FWHM}} = \left[\Delta\lambda_{\mathrm{inst}}^2 + 4\ln(2)\left(\frac{\lambda}{c}\right)^2\left(\frac{2k_{\mathrm{B}}T_{\mathrm{i}}}{M} + v_{\mathrm{nt}}^2\right)\right]^{1/2}. \quad (5)$$

Here λ is the line wavelength, c is the speed of light, and M is the mass of the ion. The instrumental width varies along the slit, and we used the calibration given by Hara et al. (2011). After accounting for the instrumental broadening it is convenient to express the line width in terms of the effective
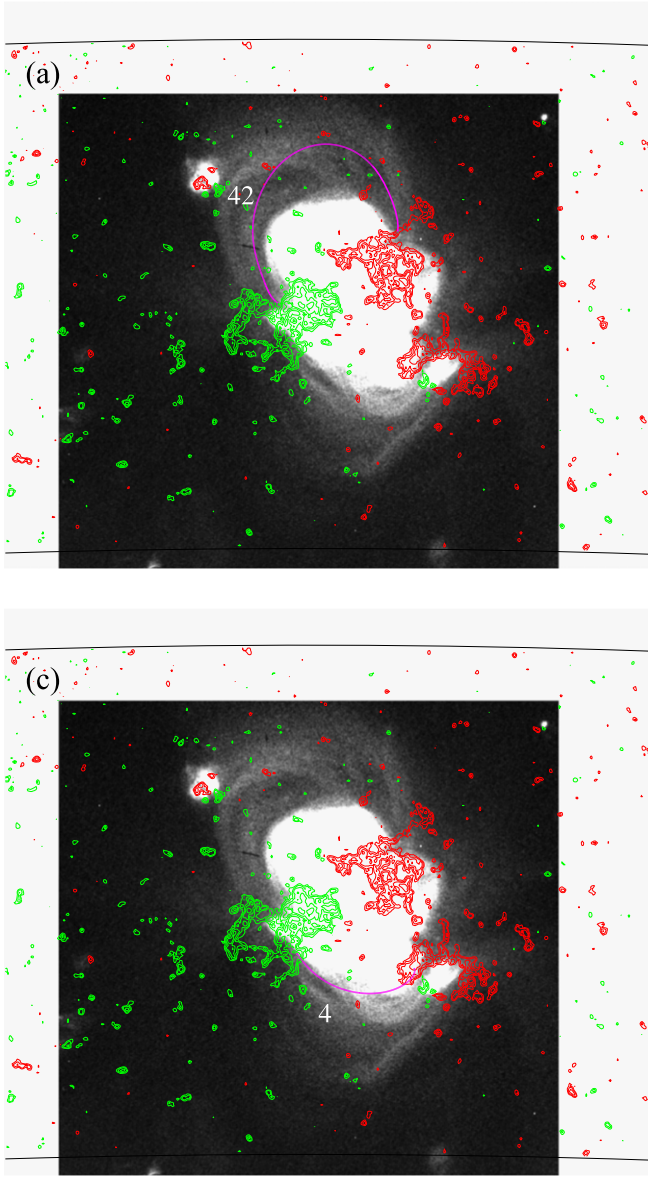
Figure 5. (a) XRT observation of active region NOAA 10938 on 2007 January 18 at 19:19:42 UT with a fitted field line, numbered 42, to the observed cloud. (b) The magnetic field variation as a function of position for field line 42. (c) The magnetic field line numbered 48 in the same active region. (d) Magnetic field variation as a function of position for field line 48.

velocity given by

$$v_{\mathrm{eff}} = \sqrt{\frac{2k_{\mathrm{B}}T_{\mathrm{i}}}{M} + v_{\mathrm{nt}}^2}. \qquad (6)$$

In order to separate the contributions from T_{i} and v_{nt} to v_{eff}, it is necessary to introduce other constraints. One reasonable assumption is that v_{nt} is the same for all of the ions. This is because the nonthermal velocity represents fluid motions that affect the entire plasma. Because all of the ions in the volume are affected in the same way, v_{nt} is independent of the particular ion species causing the emission. Using this constraint, upper and lower bounds for T_{i} can be obtained using the method of Tu et al. (1998) as follows: because v_{nt} is the same for every ion, the maximum v_{nt} that can be consistent with the observations is the full v_{eff} for the narrowest observed line. This implies that for that particular line $T_{\mathrm{i}} = 0$, though the

other, broader, lines will have nonzero T_{i}. Setting v_{nt} equal to the minimum v_{eff} gives a lower bound for T_{i} for each ion species. The upper bound for T_{i} can be found by assuming that $v_{\mathrm{nt}} = 0$.

Based on this analysis, we found that T_{i} did not exhibit any trend that depended on the ion species, such as a dependence on charge q, mass M, or charge-to-mass ratio q/M. Additionally, the range of possible ion temperatures was consistent with the electron temperature T_{e}. However, because we find only lower and upper bounds, the range of ion temperatures is broad, ranging from $\log[T\,(\mathrm{K})] \approx 6.0$ to $\log[T\,(\mathrm{K})] \approx 6.6$. Because the ion temperature is consistent with the electron temperature, it is reasonable to assume that the ions and electrons are in thermal equilibrium and that $T_{\mathrm{i}} = T_{\mathrm{e}}$ for all the ions. Henceforth, we refer to both the electron and ion temperature as T, because they are equivalent to within the measurement uncertainties.
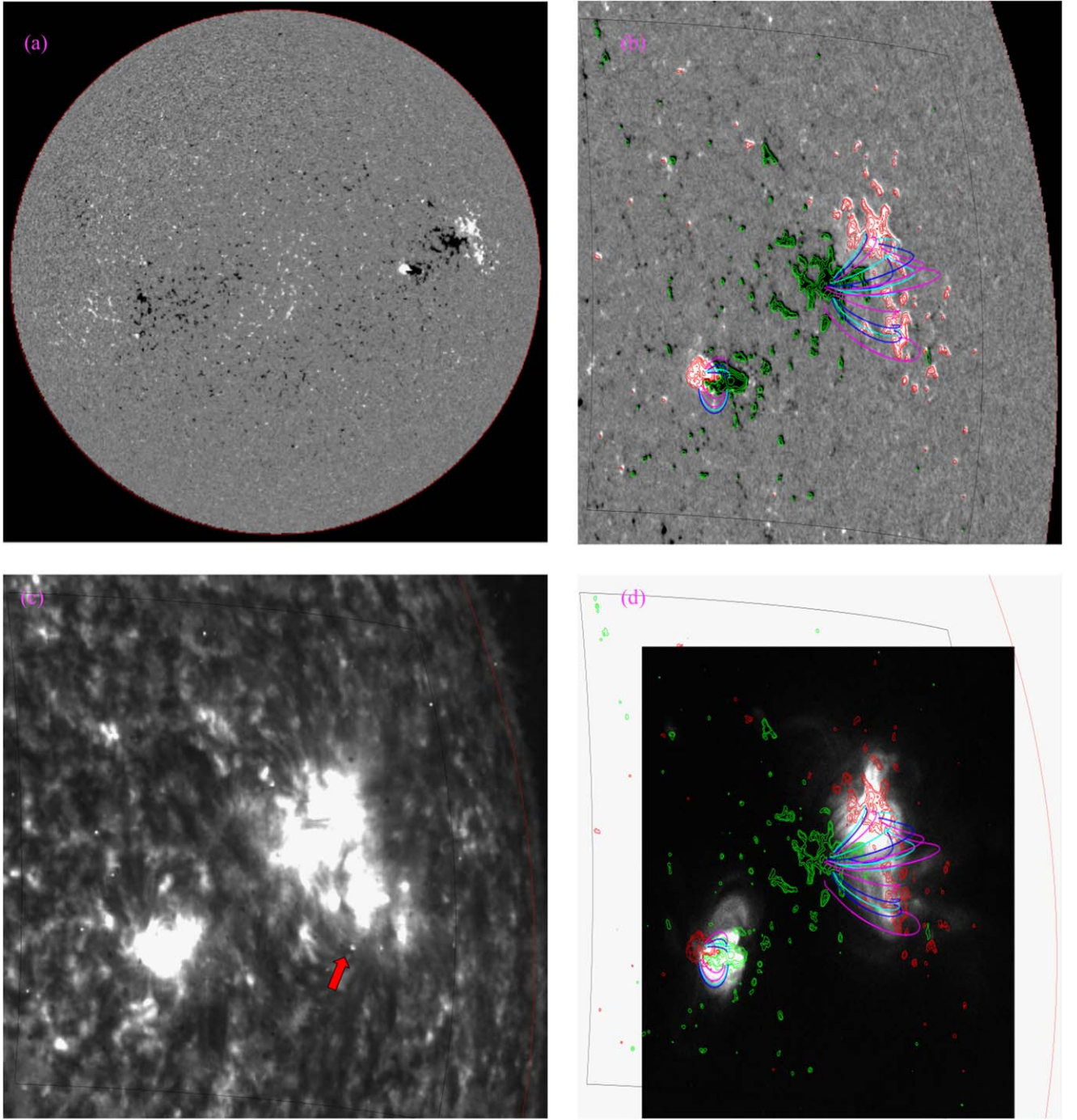
Figure 6. (a) MDI full-disk magnetogram observed on 2007 January 22 at 00:03:30 UT. (b) NLFFF model of active regions NOAA 10938 (top right) and NOAA 10939 (lower left). The curves are randomly selected field lines connecting positive and negative polarities and traced through the 3D model. (c) The active regions NOAA 10938 and NOAA 10939 observed by EIT/SOHO on 2007 January 22 at 01:19:40 UT in 304 Å with the filament (red arrow) passing through it. (d) The same magnetic field lines shown in panel (b) traced through the NLFFF model. The background image is an XRT image on 2007 January 22 at 00:03:24 UT taken with the Al-poly filter. The red curve denotes the location of the solar limb.

3.3. Temperature Gradient Length Scale

The temperature gradient length scale, L_T, was calculated from the temperature map, $T(x, y)$, illustrated in Figure 12. The length scale of the radial temperature gradient is defined by

$$L_T = \left[\frac{d \ln(T)}{dr} \right]^{-1}, \qquad (7)$$

where ln is the natural logarithm. We measured L_T in the ROI above the active region loops, so our analysis omits the strong gradients at the limb and within the active region itself. We find that the length scale falls off rather slowly with height, with $L_T = 290 \pm 90$ Mm. As our analysis discerned no difference between T_e and T_i, this estimate for L_T applies to both the electrons and the ions.
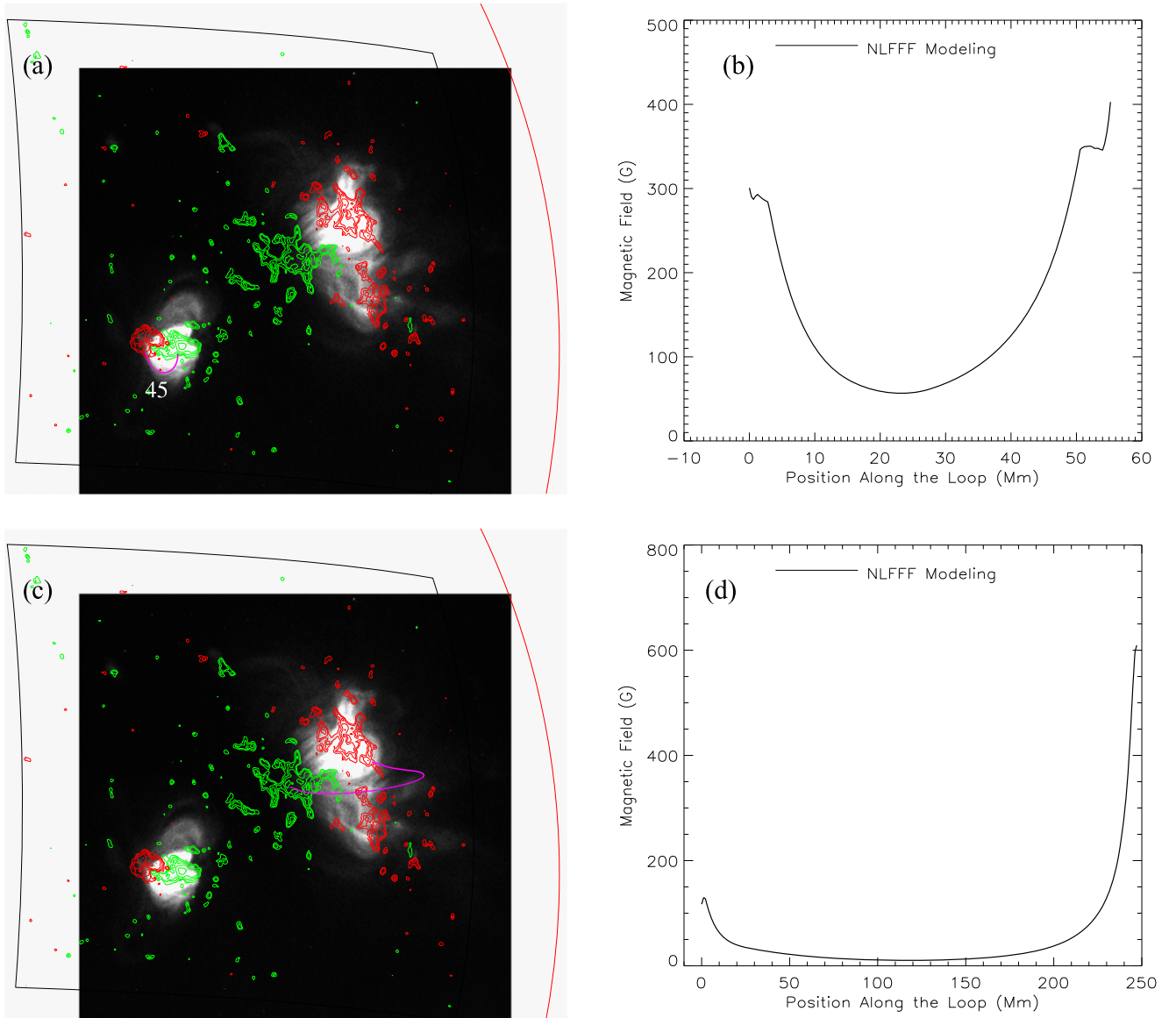
7

Figure 7. (a) XRT observation of active regions NOAA 10938 (upper right) and NOAA 10939 (lower left) on 2007 January 22 at 00:03:24 UT, with fitted field line numbered 45. The red curve denotes the location of the solar limb. (b) The magnetic field variation as a function of position for field line 45. (c) Fitted field line numbered 37. (d) Magnetic field variation as a function of position for field line 37.

3.4. Density and Density Gradient

The electron density was found using the Fe XIII density diagnostic based on the intensity ratio of the 202.04 and 203.8 Å self-blend, which includes the Fe XIII lines at 203.77, 203.80, 203.83, and 203.84 Å. The calibration relating the intensity ratio to n_e was obtained using the CHIANTI atomic database (Del Zanna et al. 2015). Figure 13 maps the density in the field of view determined using this diagnostic.

The density gradient length scale, L_n, in the ROI was estimated using an equation analogous to Equation (7), but with T replaced by n_e. We found the radial density variation has a scale length of about $L_n = 27 \pm 1$ Mm.

For a temperature of 2 MK, the hydrostatic density scale height would be about 100 Mm. The inferred density gradient length scales are about one-quarter of that. The smaller length scale may be due to the plasma not being in hydrostatic equilibrium, or the presence of unresolved structures that influence the inferred density by introducing a filling factor.

3.5. Nonthermal Velocity

The nonthermal velocity can be determined directly from Equation (6) if T_i is known. As discussed above, the ion temperatures in this observation were consistent with $T_i = T_e$ and so we can infer v_{nt}. For each pixel in the observation, we find the average v_{nt} among all the lines used earlier for the ion temperature analysis.

Figure 14 maps v_{nt} throughout the field of view in the $2''$ binned data. In the ROI above the loops, $v_{nt} \approx 20$ km s^{-1}. There appear to be large changes in v_{nt} in the other portions of the observation. On the disk, we see that there is much variation in v_{nt}. In that portion of the observation, the magnetic field lines have a lot of variation in their orientation with respect to the line of sight. The observed spread in v_{nt} is probably due to flows along those field lines. Moving to larger heights, we find that v_{nt} increases from the solar limb up to the top of the active region loops. Starting at the legs of the loops, the line of sight is primarily across the magnetic field, and v_{nt}
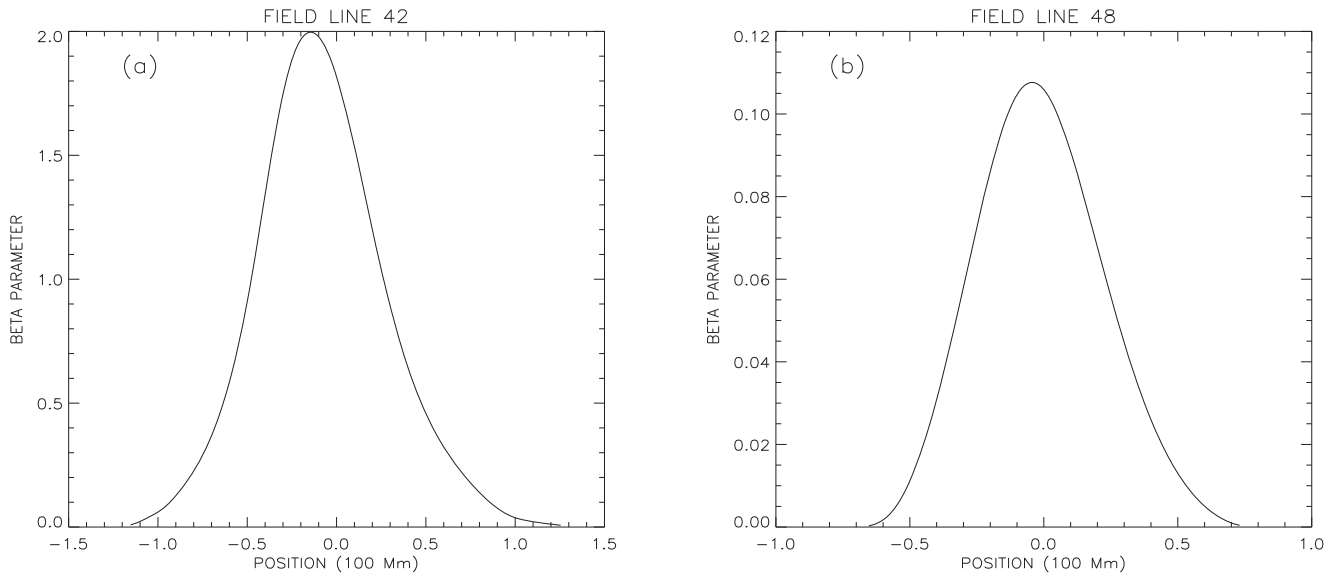
Figure 8. Plasma β parameter plotted along (a) field line 42 and (b) field line 48 shown in Figure 5.
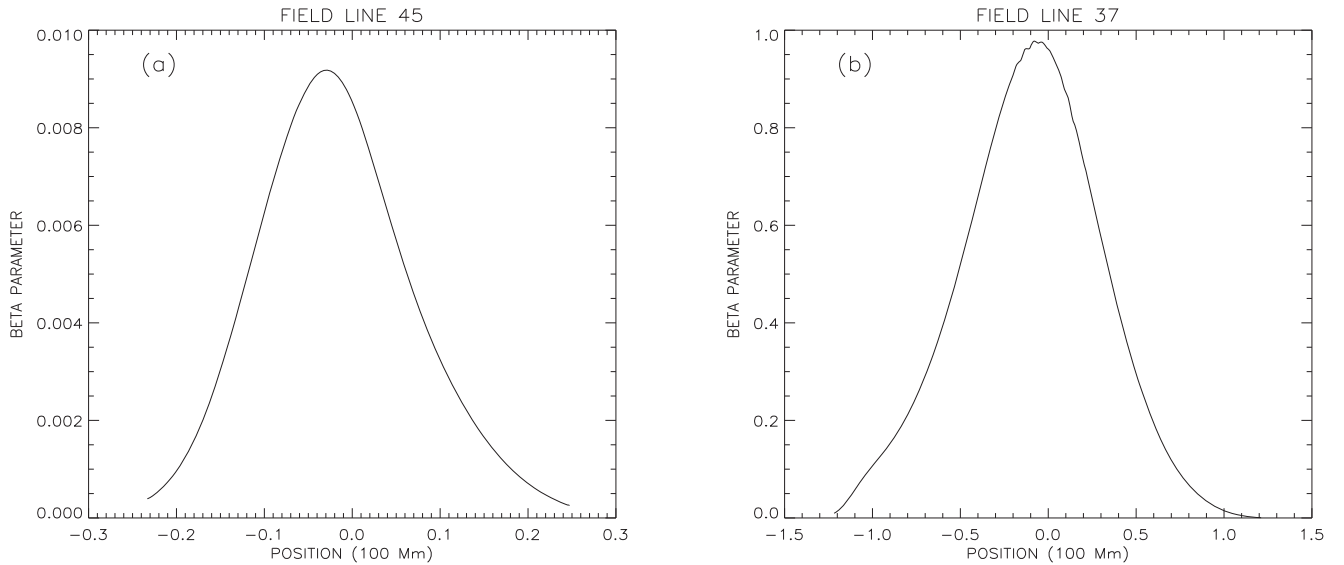

Figure 9. Plasma β parameter plotted along (a) field line 45 and (b) field line 37 shown in Figure 7.

measures broadening from turbulence and waves. At the loop top, the magnetic field turns so that the angle with the line of sight has a larger parallel component. Thus, v_{nt} at the loop top is also sensitive to parallel flows. Above the loop tops, we see that v_{nt} decreases sharply to about 20 km s^{-1}. At those heights in the ROI, the geometry of the magnetic field is uncertain and v_{nt} is likely due to waves or turbulence.

4. Discussion

We have been unable to find any references in the literature to coronal features such as the hot clouds herein analyzed. Features with some similarity were reported by Grechnev et al. (2006, p. 286): "Large-scale hot features were detected and observed several times high in the solar corona in the high-temperature Mg XII line $T = 5$–20 MK, $T_{max} = 10$ MK with the soft X-ray telescope of the SPIRIT instrumentation complex on board the CORONAS-F spacecraft. These features look like a spider and extend to heights of 300,000 km and live up to a few

days." Those features were apparently associated with coronal mass ejections and were identified as the hot upper parts of post-eruptive arcades (Kuzin et al. 2012). No such eruptive events were seen in connection with the features analyzed in the present study.

The possibility exists that the hot clouds observed here may be a coronal feature long ago known as a "coronal enhancement." An analysis of such features seen at the limb in extreme ultraviolet images (Boardman & Billings 1969) concluded that emission was seen at a height of 30,000 km, spanning 20,000 km, and with a temperature of 2–3 MK and electron density approaching 10^9 cm^{-3} (their Figure 2). The data were obtained in a brief sounding rocket flight (Tousey 1967) so that duration and time variability of the enhancement are unspecified.

The data presented here provide constraints for theoretical models of active region clouds. We believe that the $\beta \approx 1$ condition leads to a marginally stable situation such that these diffuse structures may be due to a temperature-gradient-driven
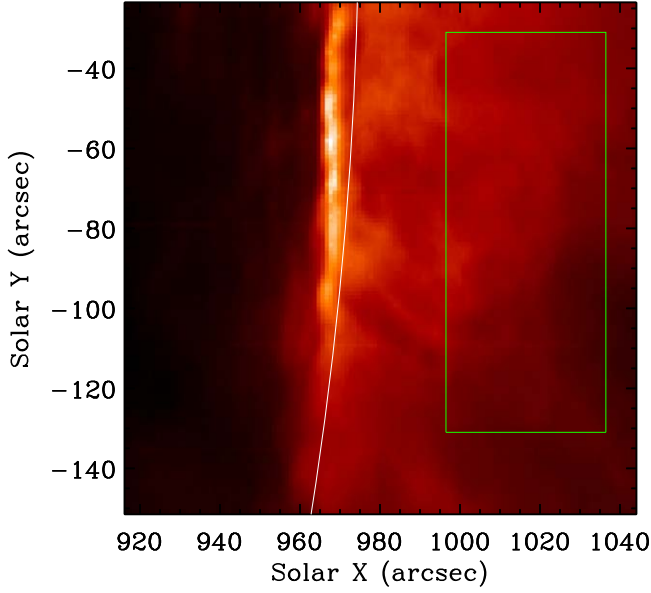
Figure 10. Image in the Fe XII 195.12 Å line intensity of the region observed by EIS on 2007 January 26 04:03:20 UT. The boxed region shows the region of interest above the active region loops selected for the analysis in Section 3. For these images, the coordinates are labeled in arcseconds from the center of the Sun and at the time of the observation, the apparent solar radius was $\approx 975''$ (as shown by the white line).
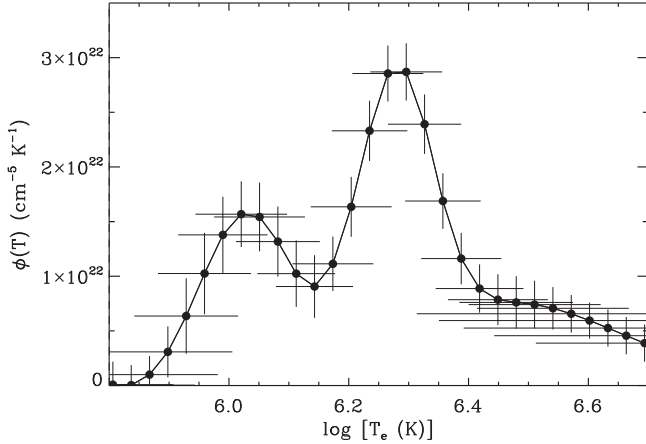

Figure 11. DEM at the coordinates $(1001'', -90''.5)$. The bimodal form of the DEM is typical throughout the observed field of view.
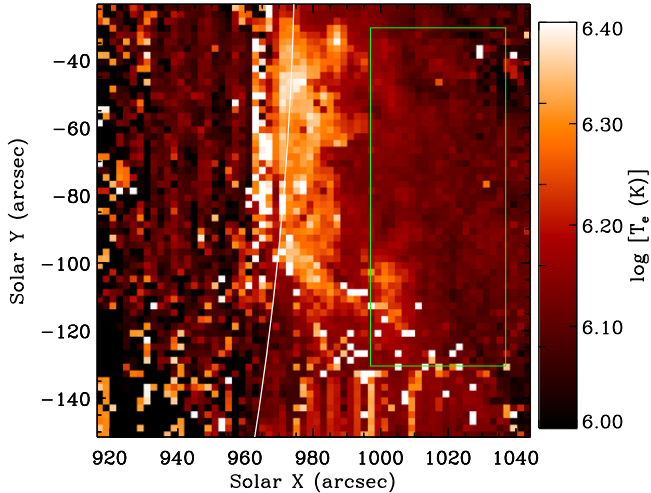
Figure 12. Map of T_e within the field of view in the $2''$ binned data.
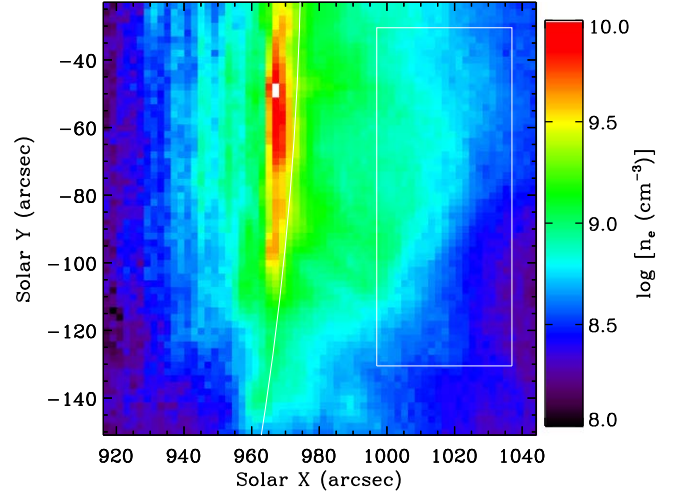
Figure 13. Map of n_e within the field of view in the $2''$ binned data.
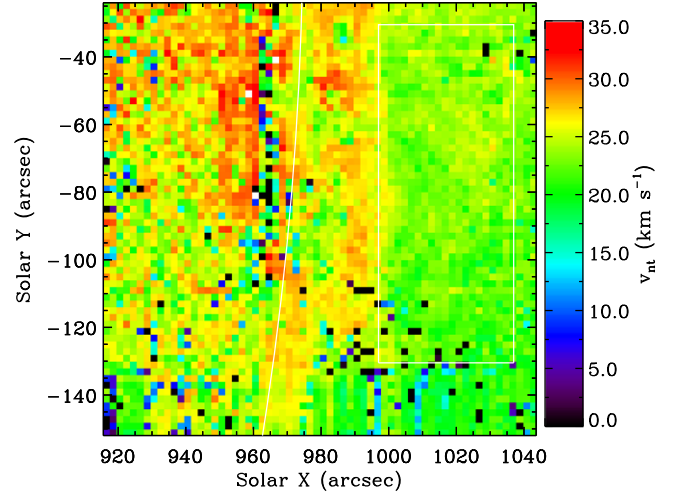

Figure 14. Map of v_{nt} within the field of view in the $2''$ binned data.

instability that introduces turbulent flows (Coppi & Spight 1978; Coppi & Sharky 1981) in the region above the active region loops. Also, the solar corona is a proton-abundant plasma (Raymond et al. 1997). In such plasma, collective modes can be excited that produce inward transport of protons while the helium nuclei and other ions are transported outward (Coppi & Spight 1978; Coppi & Sharky 1981). We hope to develop this theory further and to investigate the role of the plasma beta by conducting an analysis of these diffuse structures using observations from XRT as well as the EUV and magnetic field instruments on board the Solar Dynamics Observatory. These observations and the theory may help to explain the formation and evolution of the plasma clouds above the coronal loops.

ORCID iDs

M. Asgari-Targhi ● https://orcid.org/0000-0003-0204-8385
L. Golub ● https://orcid.org/0000-0001-9638-3082
M. Hahn ● https://orcid.org/0000-0001-7748-4179
N. Karna ● https://orcid.org/0000-0002-1314-4690
D. W. Savin ● https://orcid.org/0000-0002-1111-6610

References

Asgari-Targhi, M., & van Ballegooijen, A. A. 2012, ApJ, 746, 81
Asgari-Targhi, M., van Ballegooijen, A. A., Cranmer, S. R., & DeLuca, E. E. 2013, ApJ, 773, 111
Asgari-Targhi, M., van Ballegooijen, A. A., & Imada, S. 2014, ApJ, 786, 28
Boardman, W. J., & Billings, D. E. 1969, ApJ, 156, 731
Bobra, M. G., van Ballegooijen, A. A., & Deluca, E. E. 2008, ApJ, 672, 1209
Coppi, B., & Sharky, N. 1981, NucFu, 21, 11
Coppi, B., & Spight, C. 1978, PhRvL, 41, 551
Craig, I. J. D., McClymont, A. N., & Underwood, J. H. 1978, A&AS, 70, 1
Cranmer, S. R., & Winebarger, A. R. 2019, ARA&A, 57, 157
Culhane, J. L., Harra, L. K., James, A. M., et al. 2007, SoPh, 243, 19
De Rosa, M. L., Schrijver, C. J., Barnes, G., et al. 2009, ApJ, 696, 1780
Del Zanna, G., Dere, K. P., Young, P. R., Landi, E., & Mason, H. E. 2015, A&AS, 582, A56
Gary, G. A. 2001, SoPh, 203, 71
Golub, L., DeLuca, E., Austin, G., et al. 2007, SoPh, 243, 63
Grechnev, V. V., Kuzin, S. V., Urnov, A. M., et al. 2006, SoSyR, 40, 286
Gudiksen, B. V., & Nordlund, Å. 2005, ApJ, 618, 1031
Hannah, G. I., & Kontar, E. P. 2012, A&AS, 539, 146
Hara, H., Watanabe, T., Harra, L. K., Culhane, J. L., & Young, P. R. 2011, ApJ, 741, 107
Kosugi, T., Matsuzaki, K., Sakao, T., et al. 2007, SoPh, 243, 3
Kuzin, S. V., Bogachev, S. A., Urnov, A. M., et al. 2012, Atomic Processes in Basic and Applied Physics (Berlin: Springer), 37
Landi, E., & Feldman, U. 2008, ApJ, 672, 674
Phillips, K. J. H., Feldman, U., & Landi, E. 2008, Ultraviolet and X-ray Spectroscopy of the Solar Atmosphere (Cambridge: Cambridge Univ. Press)
Raymond, J., Kohl, J. L., Noci, G., et al. 1997, SoPh, 175, 645
Reidy, W. P., Vaiana, G. S., Zehnpfennig, T., & Giacconi, R. 1968, ApJ, 151, 333
Rosner, R., Tucker, W. H., & Vaiana, G. S. 1978, ApJ, 220, 643
Savcheva, A., & van Ballegooijen, A. A. 2009, ApJ, 703, 1766
Scherrer, P. H., Bogart, R. S., Bush, R. I., et al. 1995, SoPh, 162, 129
Schrijver, C. J., & van Ballegooijen, A. A. 2005, ApJ, 630, 552
Su, Y., Surges, V., van Ballegooijen, A., DeLuca, E., & Golub, L. 2011, ApJ, 734, 53
Su, Y. N., van Ballegooijen, A. A., Lites, B. W., et al. 2009a, ApJ, 691, 105
Su, Y. N., van Ballegooijen, A. A., Schmieder, B., et al. 2009b, ApJ, 704, 341
Tousey, R. 1967, ApJ, 149, 239
Tu, C.-Y., Marsch, E., Wilhelm, K., & Curdt, W. 1998, ApJ, 503, 475
Vaiana, G. S., & Rosner, R. 1978, ARA&A, 16, 393
van Ballegooijen, A. A. 2004, ApJ, 612, 519